Life Sciences in Space Research 26 (2020) 149–162

Contents lists available at ScienceDirect

Life Sciences in Space Research

journal homepage: www.elsevier.com/locate/lssr

CRaTER observations and permissible mission duration for human operations in deep space

Wouter C. de Wet[a,*], Tony C. Slaba[b], Fatemeh Rahmanifard[a], Jody K. Wilson[a], Andrew P. Jordan[a], Lawrence W. Townsend[c], Nathan A. Schwadron[a], Harlan E. Spence[a]

[a] University of New Hampshire Earth, Oceans, and Space Science Center, 8 College Road, Durham, NH 03824, United States
[b] NASA Langley Research Center, 1 Nasa Drive, Hampton, VA 23681, United States
[c] University of Tennessee Department of Nuclear Engineering, 1412 Circle Drive, Knoxville, TN 37916, United States

ARTICLE INFO

Keywords:
Permissible mission duration
Radiation risk
Lunar reconnaissance orbiter
Cosmic ray telescope for the effects of radiation
Solar cycle

ABSTRACT

Prolonged exposure to the galactic cosmic ray (GCR) environment is a potentially limiting factor for manned missions in deep space. Evaluating the risk associated with the expected GCR environment is an essential step in planning a deep space mission. This requires an understanding of how the local interstellar spectrum is modulated by the heliospheric magnetic field (HMF) and how observed solar activity is manifested in the HMF over time. While current GCR models agree reasonably well with measured observations of GCR flux on the first matter, they must rely on imperfect or loose correlations to describe the latter. It is more accurate to use dose rates directly measured by instruments in deep space to quantify the GCR condition for a given period of time. In this work, dose rates observed by the Cosmic Ray Telescope for the Effects of Radiation (CRaTER) instrument are used to obtain the local GCR intensity and composition as a function of time. A response function is constructed that relates observed dose rates to solar modulation potential using a series of Monte Carlo radiation transport calculations. The record of observed solar modulation potential vs. time is then used to calculate a recent historical record of permissible mission duration (PMD) according to NASA's permissible exposure limits (PEL). Tables are provided for extreme values of PMD. Additional tables include risk of exposure-induced death (at upper 95% confidence interval) accrual rates and NASA effective dose rates as a function of solar modulation potential, astronaut age, sex, and shielding thickness. The significance of the PMD values reported in relation to likely transit duration requirements for future exploration missions is discussed. There is general agreement between CRaTER observations and the prescription of solar modulation vs. time given by the Badhwar–O'Neill 2014 GCR model. However, CRaTER observations do capture the effects of significant heliospheric transients, among other features, that are missing from the prescription of solar modulation potential vs. time.

1. Introduction

NASA is working to send humans back to the moon and beyond to Mars within the next two decades (NASA Strategic Plan, 2018; Trump, 2017). The biological risks associated with extraterrestrial ionizing radiation exposures are an important factor to consider when planning human operations in deep space. In this environment, high-energy hadronic charged particles with $Z \geq 1$ penetrate spacecraft shielding and interact with biological tissue. These interactions are associated with an increased probability of carcinogenesis, mutagenesis, and cell death among other effects. The two primary natural sources of charged particle radiation in the interplanetary environment are solar energetic particles (SEP) and galactic cosmic radiation (GCR). Though they do not share a common origin, both sources of ionizing radiation are modulated by the 11-year solar cycle.

Solar energetic particles, as their name suggests, originate near the sun and are often associated with coronal mass ejections (CME) and interplanetary shock waves. SEPs, though localized spatially near the Sun, accelerate and expand into interplanetary space, eventually populating large parts of the solar system with extremely energetic ions and electrons. These events are composed primarily of H and He ions but do contain elements as heavy as Fe in observable quantities. SEP transients are more likely to occur during solar maximum and are relatively infrequent during periods of solar minimum (Kim et al., 2009). Every SEP event is unique in isotopic and energetic composition and typically lasts anywhere between hours to days for a particular location

* Corresponding author at: University of New Hampshire, 106 Morse Hall, 8 College Road, Durham, NH 03824, United States.
E-mail address: wouter.dewet@unh.edu (W.C. de Wet).

https://doi.org/10.1016/j.lssr.2020.04.004
Received 16 December 2019; Received in revised form 9 April 2020; Accepted 11 April 2020

Nomenclature

AU	Astronomical Unit
CME	Coronal Mass Ejection
CRaTER	Cosmic Ray Telescope for the Effects of Radiation
FAX	Female Adult voXel
GCR	Galactic Cosmic Radiation
HMF	Heliospheric Magnetic Field
HZETRN	High-Charge-and-Energy Particle Transport Code
ISSN	International Sunspot Number
LaRC	Langley Research Center
LET	Lineal Energy Transfer
LRO	Lunar Reconnaissance Orbiter
MAX	Male Adult voXel
MC	Monte Carlo
MCNP6	Monte Carlo N-Particle Transport Code 6
MeV	Megaelectronvolt
MV	Megavolt
Sv	Sievert
Gy	Gray
NASA	National Aeronautics and Space Administration
PEL	Permissible Exposure Limit
PMD	Permissible Mission Duration
REID	Risk of Exposure Induced Death
SEP	Solar Energetic Particle
TEP	Tissue Equivalent Plastic
Z	Charge

within the heliosphere.

The second source, GCR, is composed of high-energy ions originating from outside of the heliosphere. GCR particles originate from the shock waves of stellar supernovae (Ackermann et al., 2013), and as such have much higher energies than that of a typical SEP event. The entire periodic table of elements ranging from H through U are present within the GCR spectrum, although only species as heavy as Fe are observed in significant quantities. GCR particles from the local interstellar space are modulated by the Sun. The extension of the Sun's magnetic field produces the heliospheric magnetic field (HMF) which varies with the Sun's magnetic field strength and acts to impede and modulate GCR penetration into the inner heliosphere. The modulation of GCR particles is strongest during periods of solar maximum when the Sun's magnetic field and the HMF are strongest, and weakest during periods of solar minimum. The strength of the modulation is quantified by the so-called “modulation potential”; when modulation potential is comparatively large then GCR fluxes are comparatively low, and vice versa.

Whereas SEP events are sporadic, short-lived (order of days), and are characterized by intense flux enhancements (many orders of magnitude) particularly at relatively low energies, GCRs are ever-present, only slowly (decadal) and weakly (factors of two in dose rate) varying, with comparatively low fluxes that are extremely energetic. Both sources are important for quantifying risk factors to ionizing radiation. This study focuses on the biological risk presented by GCR ionizing radiation to astronauts traveling in interplanetary space. Due to the infrequent and unique nature of each SEP event, the risk associated with SEP radiation is not considered here.

In this work, permissible mission duration for manned operations in deep space is calculated from observations made by the Cosmic Ray Telescope for the Effects of Radiation (CRaTER). The permissible mission duration is based upon NASA's permissible exposure limits (PEL). NASA defines human radiation permissible exposure limits as a 3% risk of exposure-induced death (REID) at the upper 95% confidence interval (NASA Human Integration Design Handbook, 2014; NASA Standard 3001, Vol. 2, 2015).

2. CRaTER instrument

The Lunar Reconnaissance Orbiter (LRO) was launched on June 18, 2009, carrying CRaTER and several other exploration instruments into a polar orbit around the moon. The CRaTER instrument is a lineal energy transfer (LET) spectrometer composed of six cylindrical-disk shaped Si solid state ionizing radiation detectors and two cylindrical volumes of A-150 tissue equivalent plastic (TEP) (Spence et al., 2010). The eight components of the telescope stack are aligned along a single common cylindrical axis. The CRaTER telescope is mounted onto the LRO spacecraft such that, in the nominal operations configuration, this common axis corresponds with the direction normal to the lunar surface at the point on the surface that is closest to the spacecraft.

The six detectors are arranged into three pairs, separated by the two TEP volumes. Each pair consists of one thin detector and one thick detector and covers the entire range of LET values between 9×10^{-2} keV/μm and 2.2×10^{3} keV/μm in Si. The thicknesses along the axial dimension for thin and thick detectors are ~149 μm and 1 mm, respectively. The individual detectors within the stack are named such that odd numbers (e.g. D1, D3, D5) represent the thin detectors and even numbers (e.g. D2, D4, D6) represent the thick detectors. The two TEP volumes, T1 and T2, occupy the space between the three detector pairs such that the order of components and their corresponding axial thicknesses in the direction from zenith to nadir are: S1 (0.8128 mm), D1 (148 μm), D2 (1.0 mm), T1 (53.967 mm), D3 (149 μm), D4 (1.0 mm), T2 (11.9 mm), D5 (149 μm), D6 (1.0 mm), S2 (0.81026 mm). Components S1 and S2 refer to the Al endcaps provided by the instrument housing. A particle must therefore penetrate at least 8.44 g/cm^2 of material to pass from S1 to D6. Spence et al. (2010) provides a detailed description of the CRaTER instrument.

CRaTER is designed to perform in situ dose rate measurements of the primary GCR spectrum behind biologically significant quantities of surrogate tissue. For the purposes of this manuscript, an event occurs when a particle passes through one or more of the detectors and deposits sufficient energy within the detection volume(s) to be recognized (not identified) by the corresponding circuitry. When any valid event occurs, the corresponding energy deposited in every detector is recorded by the instrument.

An event in which multiple detectors are triggered simultaneously is flagged as a coincident event. By placing coincidence conditions on the events contributing to specific dose rate observations, one can isolate the dose rate contributions of specific components of the incident particle spectrum in both energy and direction. For example, the dose rates due to lunar albedo heavy-charged particles can be identified as events in which D6 and D4 are triggered simultaneously and in which the dose measured in D4 is greater than that in D6 (see Looper et al. (2013), Spence et al. (2013)).

Events in which detectors from all three pairs are each triggered simultaneously may only be caused by particles entering the telescope stack from either end, as opposed to side-penetrating particles or particles that have passed through the spacecraft bulk. In the case of such a triple-coincident event, the penetrating particle's average track-length through each detector is known. The recorded energy deposition for each triggered detector can then be converted to a measured LET. The dose for the entire detector pair may be obtained using the measured LET of a single triggered detector within the pair. Because of the overlap in the detectable LET ranges of the thin and thick detectors in each pair, either or both detectors in a given pair may be triggered for any given event. If both detectors in a pair are triggered during an event, the measured LET from either is selected to calculate the dose for the detector pair.

The incident particle of a triple-coincident event is known to have entered from the free space end if the LET measured in the third pair (D5, D6) is greater than the LET measured in the second pair (D3, D4), which must subsequently be greater than the LET measured in the first pair (D1, D2). In this study, the above technique is used to identify the dose rates in the third detector pair (D5, D6) by a population of GCR particles that enter the detector telescope from deep space.

3. Modeled crater response function

A response function is required to relate the GCR boundary condition with the dose rates observed by the CRaTER instrument. The Monte Carlo N-Particle 6 (MCNP6) radiation transport code (Goorley et al., 2012) is used to calculate the response function. This general-purpose Monte Carlo transport code transports photons, neutrons, electrons, protons, and heavy charged particles through complex geometries. The results of twenty independent calculations on the same geometry are used to assemble the response function.

Each calculation is performed with a unique boundary condition representing the entire charged particle component of the GCR spectrum for a specific solar modulation potential value. The solar modulation potential values that are considered in this work range between 420 MV (solar minimum) and 2400 MV (solar maximum). The GCR boundary conditions are obtained using the Badhwar–O'Neill 2014 prescription of solar modulation, which solves the Fokker-Planck equations to transport the local interstellar spectrum to 1 AU (O'Neill et al., 2015). The GCR boundary flux includes 28 charged particle species from H through Ni with incident energies ranging from 1×10^{-1}A MeV through 1×10^{4}A MeV.

Incident particles are sampled on a spherical shell surrounding the telescope geometry such that they represent an isotropic field of GCR particles in deep space. The telescope geometry includes the six cylindrical Si detectors, the two cylindrical TEP volumes, and the aluminum shielding at each end. This geometry, in combination with the coincidence requirements imposed on the tallied quantities, is sufficient to physically represent the observations used in this study. These observations are discussed in greater detail in the following section.

The absorbed dose in the third detector pair is tallied in the simulation. However, only particles that pass into the third detector pair after passing through the first pair may contribute to the absorbed dose tally. This ensures that only particles entering from the free-space end of the telescope are counted in the simulation. Excellent agreement in all six detectors has been demonstrated between CRaTER observations and modeled results produced using the MC transport code High Energy Transport Code – Human Exploration and Development of Space (HETC–HEDS) for heavy charged particles with energies ranging from 20A MeV through 3×10^{3}A MeV (Townsend et al., 2010). It then follows that such an approach is appropriate to accurately quantify the instrument response for the entire ensemble of GCR isotopes and energies.

The absorbed dose response function, illustrated in Fig. 1, is smooth and decreases exponentially with increasing solar modulation potential. The behavior of the response function is driven by the decrease in GCR flux associated with increasing modulation potential. Interpolating this response function gives the expected dose rate observed by CRaTER for any value of solar modulation potential. Conversely, one may also use the dose rate observed by CRaTER to obtain the average solar modulation potential for any particular time period.

The inherent assumptions associated with this approach introduce a notable restriction. The relationship between solar modulation potential and GCR flux is model dependent. In other words, two independent GCR models would attribute different values of solar modulation potential to any given GCR condition. Furthermore, while the two models will likely have two very different timeseries prescriptions of solar modulation potential over a given period, the resulting GCR spectra obtained when evaluating each for a given date should be very similar. Therefore, any interpretation or analysis of the results obtained using this response function must also adhere to the Badhwar–O'Neill 2014 definition of solar modulation potential for a given GCR flux.

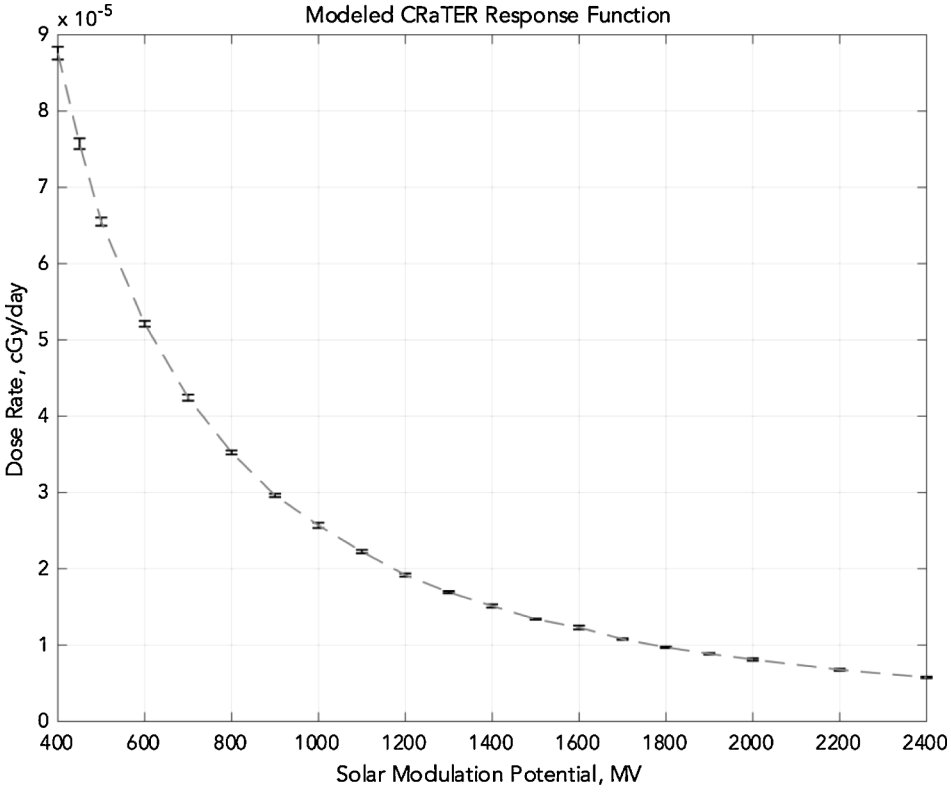

Fig. 1. Modeled CRaTER Response Function. The modeled absorbed dose rate in Si for the third detector pair (D5, D6) with coincidence and increasing LET requirements in the first pair (D1, D2) and second pair (D3, D4) as a function of Badhwar–O'Neill 2014 solar modulation potential. The error bars represent modeled datapoints and carry the statistical uncertainty in the MCNP6 calculation. The dashed line is an interpolation of the modeled data points.

4. CRaTER observations

In this section, the process for extracting observed dose rates of interest from the archive of CRaTER data is described. Additionally, the observed dose rates are compared with the expected values calculated using the Badhwar–O'Neill 2014 timeseries prescription for solar modulation potential. The response function described in the previous section is designed to represent a specific measurement extracted from CRaTER observations: the absorbed dose rate in the third detector pair (D5, D6) for particles that have also passed through both the first (D1, D2) and second (D3, D4) detector pairs, with the added requirement that the measured LET increases in each subsequent detector pair. The requirement of increasing LET filters out all events in which the incident particle is not moving from the zenith end to the nadir of the telescope.

By requiring coincidence in all three detector pairs, we limit both the field of view and the energies of the particles contributing to the dose rate. First, particles must enter the telescope from deep space through a 31.4° conical field-of-view. Selecting this limited field of incident particles ensures that all particles entering the detector have traveled through the minimum, and most uniform amount of shielding (0.2195 g/cm^2 Al) possible before passing through the detector stack. Consequently, a proton, for example, requires 114.5 MeV of kinetic energy upon entering the zenith end of the telescope to reach D6. The corresponding minimum ionizing energy for all three detector pairs is roughly 2 GeV (Spence et al., 2010). Incident GCR particles within this range of energies are sensitive to variations in solar modulation potential across the solar cycle and are also biologically relevant.

The archive of recorded CRaTER events is processed into daily averages of the observed CRaTER dose rate for the entire duration of the LRO mission to date, as illustrated in Fig. 2. The observed daily values are given as scattered data points. A Gaussian-weighted moving average with a window of 180 days, shown in orange, is applied to the daily data to eliminate the high-frequency variations and significant outliers. Plotted in blue is the expected result calculated by applying the CRaTER response function for the solar modulation potential timeseries as defined by the Badhwar–O'Neill 2014 model.

The variance in the high-cadence daily data is due to the stochastic nature of GCR incidence as well as the effects of solar-born transients within the inner heliosphere. Solar energetic particle events that cross directly over LRO's path yield unusually high dose rates over short periods of time. For the large events, this elevated dose rate may still be observed more than 10 days beyond the initial onset of the event. The selected window of 180 days is sufficient to minimize the elevated dose rates from long-lived solar energetic particle events. Further evidence of large-scale heliospheric transients also appears in the observed data. One example is the dramatic decrease following the September 2017 series of CMEs (Luhmann et al., 2018; Matthiä et al., 2018; Schwadron et al., 2018), which is manifested in Fig. 2 as an anomalous decrease in the observed dose rate over a period of roughly 180 days.

As discussed in the previous section, the CRaTER dose rate response function may also be used to extract the average modulation potential given the observed dose rate. The modulation potential timeseries data corresponding to the dose rates observed by CRaTER are illustrated in Fig. 3, along with the aforementioned timeseries from the Badhwar–O'Neill 2014 model. While there is general agreement with the observed values, there are some important differences. The Badhwar–O'Neill 2014 modulation timeseries uses monthly-average smoothed international sunspot number (ISSN) to describe the level of solar activity and a time delay of up to 14 months to allow for the effects to propagate throughout the heliosphere (O'Neill et al., 2015). This approach has a few key advantages and disadvantages. The advantages include the ability to predict future modulation potentials as well as extrapolate into the distant past as far as the year 1750. The disadvantage of this approach is that ISSN is only loosely correlated with GCR modulation potential (Iskra et al., 2019; Nymmik and Suslov, 1995; Usoskin et al., 1998). This relationship is periodically insufficient to describe anomalous behavior such as the sustained perturbation in modulation potential caused by the September 2017 series of events. Another example is the relatively weak modulation potential observed by CRaTER in the period between mid-2011 and late 2012 in comparison to the modulation potential expected according to the relatively high number of sunspots for that period.

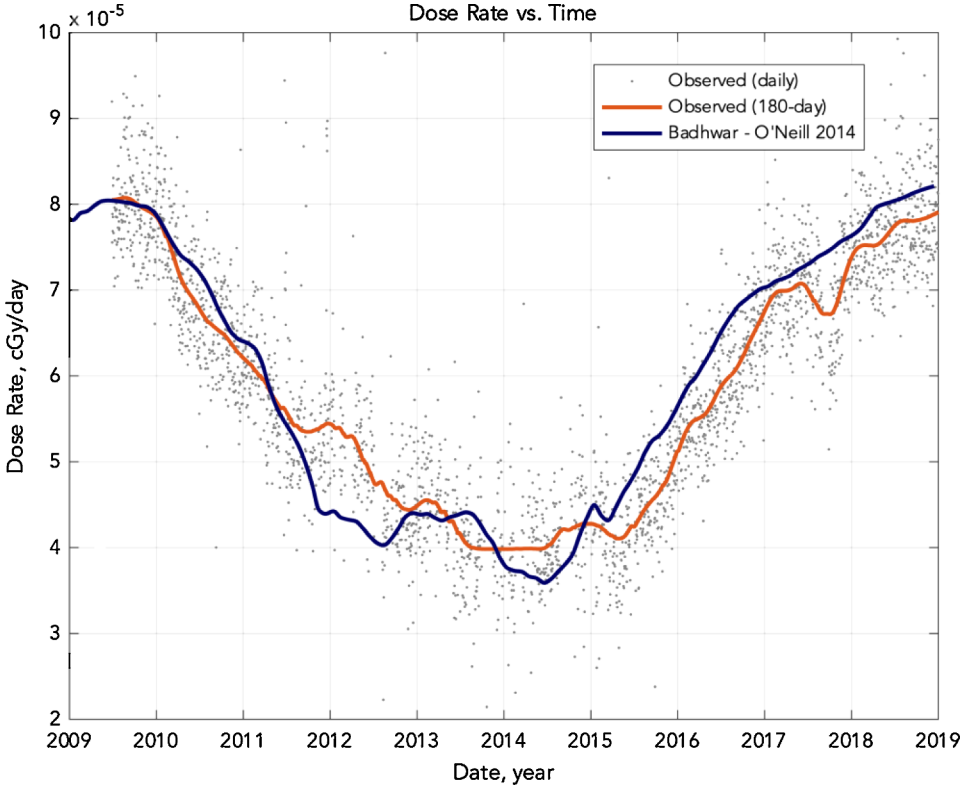

Fig. 2. Dose Rate vs. Time. The daily (points) and 180-day average (orange) absorbed dose rates observed by CRaTER in the third detector pair (D5, D6) with coincidence and increasing LET requirements in the first pair (D1, D2) and second pair (D3, D4) are compared with the expected dose rate calculated using the Badhwar–O'Neill 2014 model (blue).

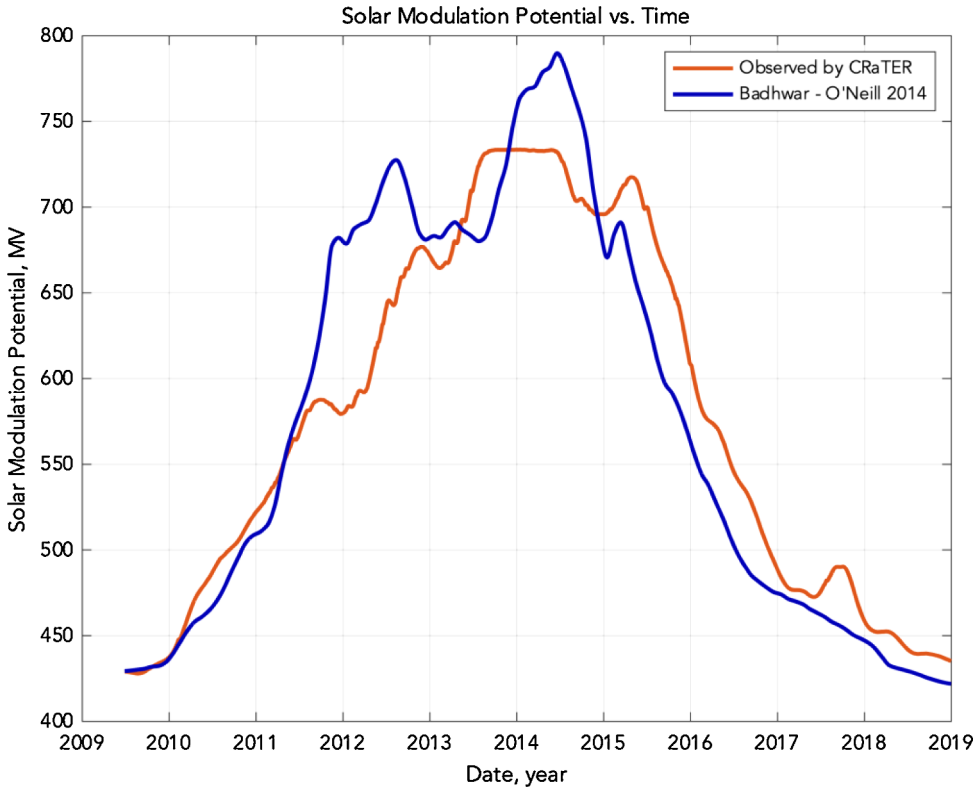

Fig. 3. Solar Modulation Potential vs. Time. The CRaTER observed solar modulation potential (orange) is compared with the timeseries defined by the Badhwar–O'Neill 2014 model (blue) for solar cycle 24.

CRaTER provides an in-situ measurement of solar modulation potential in a deep space environment. Furthermore, the primary GCR condition is observed as an absorbed dose rate behind the biologically significant shielding depth typical of human blood forming organs over an entire solar cycle (Spence et al., 2010). Consequently, this means the response observed by CRaTER over the course of the solar cycle is well suited to provide a risk estimate.

5. Risk model

In this work, the risk incurred by GCR exposure for extended human operations in deep space at 1 AU is studied as a function of an astronaut's sex, age at exposure, and spacecraft shielding thickness. NASA's deterministic transport code, the High-Charge-and-Energy Particle Transport Code (HZETRN), (Wilson et al., 1991; Slaba et al., 2010b,c) is used to calculate the NASA effective dose rate and REID for each permutation of sex, shielding thickness, and solar modulation potential. The HZETRN code has been validated against other transport codes and observational datasets (Norbury et al., 2017; Slaba et al., 2017; Matthiä et al., 2017; Warner et al., 2018). The Male Adult voXel (MAX) and Female Adult voXel (FAX) geometric phantoms, placed in a spherical spacecraft, were used to represent the male and female astronauts for all ages (Kramer et al., 2003, Kramer et al., 2004; Slaba et al., 2010a). The five ages considered range from 30 years to 50 years in increments of 5 years. The eight spherical Al spacecraft thicknesses are 0.1 g/cm^2, 0.4 g/cm^2, 1.0 g/cm^2, 2.0 g/cm^2, 5.0 g/cm^2, 10.0 g/cm^2, 20.0 g/cm^2, and 40 g/cm^2. The solar modulation potential used for the risk assessment calculation ranges between 420 MV and 1400 MV, which includes all known historic values as defined by the Badhwar–O'Neill 2014 model. The NASA effective dose rates, given in Tables 1 and 2, are calculated for never-smoker populations using NASA's quality factors (Q-values) and tissue-weighting factors (Cucinotta et al., 2013; NASA Human Integration Design Handbook, 2014). The REID calculations were performed using the 2012 version of the NASA cancer risk model (Cucinotta et al., 2013) with corrected sampling algorithms used in the probabilistic evaluation. Tables 3–12 provide REID accumulation rates at the upper 95% confidence interval as a function of astronaut sex, age at exposure, spacecraft shielding thickness, and solar modulation potential.

The term REID accumulation rate refers to the increase in total risk of exposure induced death from a particular exposure received over a given time period. Fig. 4 illustrates the REID accumulation rate at the upper 95%

Table 1
NASA effective dose rates, in mSv/day, for male astronauts (MAX) as a function of Al shielding thickness and solar modulation potential.

Al	Solar Modulation Potential, MV										
g/cm^2	420	500	600	700	800	900	1000	1100	1200	1300	1400
0.1	1.2071	1.0309	0.8638	0.7366	0.6370	0.5572	0.4920	0.4380	0.3927	0.3543	0.3213
0.4	1.1999	1.0252	0.8594	0.7333	0.6344	0.5550	0.4903	0.4366	0.3915	0.3533	0.3205
1	1.1860	1.0142	0.8511	0.7267	0.6292	0.5509	0.4869	0.4338	0.3892	0.3514	0.3189
2	1.1646	0.9972	0.8380	0.7165	0.6210	0.5443	0.4815	0.4294	0.3856	0.3483	0.3163
5	1.1108	0.9543	0.8049	0.6904	0.6001	0.5274	0.4677	0.4180	0.3761	0.3403	0.3096
10	1.0472	0.9034	0.7654	0.6591	0.5750	0.5070	0.4510	0.4042	0.3647	0.3309	0.3018
20	0.9787	0.8493	0.7242	0.6272	0.5500	0.4872	0.4353	0.3918	0.3549	0.3232	0.2958
40	0.9463	0.8288	0.7136	0.6232	0.5506	0.4911	0.4415	0.3996	0.3639	0.3331	0.3063

Table 2
NASA effective dose rates, in mSv/day, for female astronauts (FAX) as a function of Al shielding thickness and solar modulation potential.

Al	Solar Modulation Potential, MV										
g/cm^2	420	500	600	700	800	900	1000	1100	1200	1300	1400
0.1	1.4004	1.1910	0.9934	0.8438	0.7271	0.6340	0.5582	0.4957	0.4434	0.3991	0.3613
0.4	1.3895	1.1825	0.9870	0.8389	0.7233	0.6310	0.5558	0.4937	0.4417	0.3977	0.3601
1	1.3686	1.1662	0.9748	0.8295	0.7159	0.6250	0.5510	0.4898	0.4385	0.3950	0.3578
2	1.3366	1.1411	0.9558	0.8147	0.7042	0.6156	0.5434	0.4835	0.4333	0.3907	0.3542
5	1.2573	1.0782	0.9075	0.7768	0.6739	0.5911	0.5233	0.4669	0.4194	0.3791	0.3444
10	1.1651	1.0041	0.8497	0.7309	0.6369	0.5609	0.4984	0.4462	0.4021	0.3645	0.3321
20	1.0663	0.9248	0.7881	0.6821	0.5977	0.5292	0.4725	0.4250	0.3847	0.3501	0.3202
40	1.0167	0.8898	0.7655	0.6681	0.5899	0.5258	0.4724	0.4274	0.3890	0.3559	0.3271

Table 3
REID (upper 95% confidence interval) accumulation rates, in %/day, for male astronauts exposed at an age of 30 years as a function of Al shielding thickness and solar modulation potential.

Al	Solar Modulation Potential, MV										
g/cm^2	420	500	600	700	800	900	1000	1100	1200	1300	1400
0.1	0.0148	0.0128	0.0108	0.0093	0.0081	0.0071	0.0063	0.0056	0.0050	0.0045	0.0041
0.4	0.0148	0.0127	0.0107	0.0092	0.0080	0.0070	0.0062	0.0056	0.0050	0.0045	0.0041
1	0.0146	0.0126	0.0106	0.0091	0.0079	0.0070	0.0062	0.0055	0.0050	0.0045	0.0041
2	0.0143	0.0124	0.0105	0.0090	0.0078	0.0069	0.0061	0.0055	0.0049	0.0044	0.0040
5	0.0137	0.0118	0.0100	0.0086	0.0075	0.0067	0.0059	0.0053	0.0048	0.0043	0.0039
10	0.0130	0.0113	0.0096	0.0083	0.0073	0.0064	0.0057	0.0051	0.0046	0.0042	0.0039
20	0.0122	0.0106	0.0091	0.0079	0.0069	0.0061	0.0055	0.0050	0.0045	0.0041	0.0037
40	0.0116	0.0102	0.0088	0.0077	0.0068	0.0061	0.0055	0.0050	0.0045	0.0041	0.0038

Table 4
REID (upper 95% confidence interval) accumulation rates, in %/day, for female astronauts exposed at an age of 30 years as a function of Al shielding thickness and solar modulation potential.

Al	Solar Modulation Potential, MV										
g/cm^2	420	500	600	700	800	900	1000	1100	1200	1300	1400
0.1	0.0232	0.0199	0.0167	0.0143	0.0124	0.0109	0.0096	0.0086	0.0077	0.0070	0.0063
0.4	0.0230	0.0198	0.0166	0.0142	0.0124	0.0108	0.0096	0.0086	0.0077	0.0069	0.0063
1	0.0227	0.0196	0.0165	0.0141	0.0123	0.0108	0.0095	0.0085	0.0076	0.0069	0.0063
2	0.0223	0.0192	0.0162	0.0139	0.0121	0.0106	0.0094	0.0084	0.0076	0.0068	0.0062
5	0.0211	0.0183	0.0155	0.0134	0.0117	0.0103	0.0091	0.0082	0.0073	0.0067	0.0061
10	0.0195	0.0170	0.0145	0.0126	0.0110	0.0097	0.0087	0.0078	0.0070	0.0064	0.0058
20	0.0177	0.0155	0.0133	0.0116	0.0102	0.0091	0.0081	0.0073	0.0066	0.0060	0.0055
40	0.0169	0.0149	0.0129	0.0113	0.0099	0.0089	0.0080	0.0072	0.0066	0.0060	0.0055

Table 5
REID (upper 95% confidence interval) accumulation rates, in %/day, for male astronauts exposed at an age of 35 years as a function of Al shielding thickness and solar modulation potential.

Al	Solar Modulation Potential, MV										
g/cm^2	420	500	600	700	800	900	1000	1100	1200	1300	1400
0.1	0.0142	0.0122	0.0103	0.0089	0.0077	0.0068	0.0060	0.0053	0.0048	0.0043	0.0039
0.4	0.0141	0.0121	0.0102	0.0088	0.0077	0.0067	0.0060	0.0053	0.0048	0.0043	0.0039
1	0.0139	0.0120	0.0101	0.0087	0.0076	0.0067	0.0059	0.0053	0.0047	0.0043	0.0039
2	0.0137	0.0118	0.0100	0.0086	0.0075	0.0066	0.0058	0.0052	0.0047	0.0042	0.0039
5	0.0130	0.0112	0.0096	0.0083	0.0072	0.0063	0.0056	0.0050	0.0045	0.0041	0.0038
10	0.0124	0.0107	0.0091	0.0079	0.0069	0.0061	0.0054	0.0049	0.0044	0.0040	0.0037
20	0.0116	0.0101	0.0086	0.0075	0.0066	0.0058	0.0052	0.0047	0.0043	0.0039	0.0036
40	0.0110	0.0097	0.0084	0.0073	0.0065	0.0058	0.0052	0.0047	0.0043	0.0039	0.0036

confidence interval for 45-year-old astronauts as a function of sex, shielding thickness, and solar modulation potential. Solar modulation potential, spacecraft shielding configuration, as well as astronaut sex and age at exposure each affect the magnitude of risk associated with a given GCR exposure. It is, therefore, important to investigate the influence of each variable within the context of the other three.

Three of the trends manifested in the risk model are evident in Fig. 4. The first trend is that REID accumulation rate decreases with increasing solar modulation potential. Total GCR flux is highest during solar minimum and decreases as solar modulation potential increases. The second trend is that risk accumulation rate decreases as spacecraft shielding thickness increases. Thickening aluminum spacecraft shielding converts increasingly larger fractions of the high-LET heavy charged nuclei in the incident GCR spectrum to lower-LET light ions and nucleons with relatively low biological effectiveness. The third trend is that the risk accumulation rate for females is higher than that of

Table 6
REID (upper 95% confidence interval) accumulation rates, in %/day, for female astronauts exposed at an age of 35 years as a function of Al shielding thickness and solar modulation potential.

Al	Solar Modulation Potential, MV										
g/cm^2	420	500	600	700	800	900	1000	1100	1200	1300	1400
0.1	0.0217	0.0186	0.0157	0.0134	0.0116	0.0102	0.0090	0.0081	0.0072	0.0065	0.0059
0.4	0.0216	0.0185	0.0156	0.0134	0.0116	0.0102	0.0090	0.0080	0.0072	0.0065	0.0059
1	0.0213	0.0183	0.0155	0.0132	0.0115	0.0101	0.0089	0.0080	0.0072	0.0065	0.0059
2	0.0209	0.0180	0.0152	0.0131	0.0114	0.0100	0.0088	0.0079	0.0071	0.0064	0.0058
5	0.0198	0.0170	0.0144	0.0125	0.0109	0.0096	0.0085	0.0076	0.0069	0.0062	0.0057
10	0.0183	0.0159	0.0136	0.0117	0.0103	0.0091	0.0081	0.0073	0.0066	0.0060	0.0054
20	0.0166	0.0146	0.0125	0.0109	0.0096	0.0085	0.0076	0.0069	0.0062	0.0057	0.0052
40	0.0159	0.0139	0.0120	0.0105	0.0093	0.0083	0.0075	0.0068	0.0062	0.0056	0.0052

Table 7
REID (upper 95% confidence interval) accumulation rates, in %/day, for male astronauts exposed at an age of 40 years as a function of Al shielding thickness and solar modulation potential.

Al	Solar Modulation Potential, MV										
g/cm^2	420	500	600	700	800	900	1000	1100	1200	1300	1400
0.1	0.0135	0.0116	0.0098	0.0084	0.0073	0.0064	0.0057	0.0051	0.0045	0.0041	0.0037
0.4	0.0134	0.0115	0.0097	0.0084	0.0073	0.0064	0.0057	0.0050	0.0045	0.0041	0.0037
1	0.0132	0.0114	0.0096	0.0083	0.0072	0.0063	0.0056	0.0050	0.0045	0.0041	0.0037
2	0.0130	0.0112	0.0095	0.0082	0.0071	0.0062	0.0055	0.0050	0.0045	0.0040	0.0037
5	0.0124	0.0107	0.0091	0.0078	0.0068	0.0060	0.0053	0.0048	0.0043	0.0039	0.0036
10	0.0117	0.0101	0.0086	0.0075	0.0065	0.0058	0.0052	0.0046	0.0042	0.0038	0.0035
20	0.0110	0.0096	0.0082	0.0071	0.0062	0.0055	0.0050	0.0045	0.0040	0.0037	0.0034
40	0.0106	0.0093	0.0080	0.0070	0.0062	0.0056	0.0050	0.0045	0.0041	0.0038	0.0035

Table 8
REID (upper 95% confidence interval) accumulation rates, in %/day, for female astronauts exposed at an age of 40 years as a function of Al shielding thickness and solar modulation potential.

Al	Solar Modulation Potential, MV										
g/cm^2	420	500	600	700	800	900	1000	1100	1200	1300	1400
0.1	0.0204	0.0176	0.0148	0.0126	0.0109	0.0096	0.0085	0.0075	0.0068	0.0061	0.0056
0.4	0.0203	0.0174	0.0147	0.0125	0.0109	0.0095	0.0084	0.0075	0.0068	0.0061	0.0055
1	0.0200	0.0172	0.0145	0.0124	0.0108	0.0095	0.0084	0.0075	0.0067	0.0061	0.0055
2	0.0196	0.0169	0.0143	0.0122	0.0106	0.0093	0.0083	0.0074	0.0066	0.0060	0.0054
5	0.0185	0.0160	0.0136	0.0117	0.0102	0.0090	0.0080	0.0071	0.0064	0.0058	0.0053
10	0.0173	0.0149	0.0127	0.0110	0.0096	0.0085	0.0076	0.0068	0.0061	0.0056	0.0051
20	0.0156	0.0136	0.0117	0.0102	0.0090	0.0080	0.0071	0.0064	0.0058	0.0053	0.0048
40	0.0149	0.0131	0.0113	0.0099	0.0088	0.0078	0.0070	0.0064	0.0058	0.0053	0.0049

Table 9
REID (upper 95% confidence interval) accumulation rates, in %/day, for male astronauts exposed at an age of 45 years as a function of Al shielding thickness and solar modulation potential.

Al	Solar Modulation Potential, MV										
g/cm^2	420	500	600	700	800	900	1000	1100	1200	1300	1400
0.1	0.0128	0.0110	0.0093	0.0080	0.0069	0.0061	0.0054	0.0048	0.0043	0.0039	0.0035
0.4	0.0127	0.0109	0.0092	0.0079	0.0069	0.0060	0.0053	0.0048	0.0043	0.0039	0.0035
1	0.0126	0.0108	0.0092	0.0079	0.0068	0.0060	0.0053	0.0047	0.0043	0.0039	0.0035
2	0.0123	0.0106	0.0090	0.0077	0.0067	0.0059	0.0052	0.0047	0.0042	0.0038	0.0035
5	0.0118	0.0102	0.0086	0.0074	0.0065	0.0057	0.0051	0.0046	0.0041	0.0037	0.0034
10	0.0111	0.0096	0.0082	0.0071	0.0062	0.0055	0.0049	0.0044	0.0040	0.0036	0.0033
20	0.0103	0.0090	0.0077	0.0067	0.0059	0.0052	0.0047	0.0042	0.0038	0.0035	0.0032
40	0.0100	0.0088	0.0076	0.0066	0.0059	0.0052	0.0047	0.0043	0.0039	0.0036	0.0033

males for a given age, solar modulation potential, and shielding configuration. In the case of a 45-year-old astronaut, the risk accumulation rate for females is roughly 1.5 times higher than for males. The two most significant factors responsible for the disparity in risk between the sexes are (1) the increased risk of lung cancer incidence for females as observed in the Life Span Study of atomic bomb survivors (Boice et al., 2019), and (2) the added risk of breast cancer incidence for females in comparison to males (Mossman, 2012).

Variations in the NASA effective doses corresponding to the PEL also serve to demonstrate the behavior of the risk model as a function of each variable. Fig. 5 shows the NASA effective dose required to reach the PEL for the male and female astronauts, grouped by age, as a

Table 10
REID (upper 95% confidence interval) accumulation rates, in %/day, for female astronauts exposed at an age of 45 years as a function of Al shielding thickness and solar modulation potential.

Al	Solar Modulation Potential, MV										
g/cm^2	420	500	600	700	800	900	1000	1100	1200	1300	1400
0.1	0.0193	0.0165	0.0139	0.0119	0.0103	0.0090	0.0080	0.0071	0.0064	0.0058	0.0052
0.4	0.0191	0.0164	0.0138	0.0118	0.0103	0.0090	0.0079	0.0071	0.0064	0.0057	0.0052
1	0.0189	0.0162	0.0137	0.0117	0.0102	0.0089	0.0079	0.0070	0.0063	0.0057	0.0052
2	0.0184	0.0159	0.0134	0.0115	0.0100	0.0088	0.0078	0.0069	0.0062	0.0056	0.0051
5	0.0174	0.0151	0.0128	0.0110	0.0096	0.0084	0.0075	0.0067	0.0060	0.0055	0.0050
10	0.0162	0.0140	0.0120	0.0104	0.0090	0.0080	0.0071	0.0064	0.0058	0.0052	0.0048
20	0.0147	0.0128	0.0110	0.0096	0.0084	0.0074	0.0067	0.0060	0.0055	0.0050	0.0046
40	0.0140	0.0123	0.0107	0.0093	0.0082	0.0073	0.0066	0.0060	0.0055	0.0050	0.0046

Table 11
REID (upper 95% confidence interval) accumulation rates, in %/day, for male astronauts exposed at an age of 50 years as a function of Al shielding thickness and solar modulation potential.

Al	Solar Modulation Potential, MV										
g/cm^2	420	500	600	700	800	900	1000	1100	1200	1300	1400
0.1	0.0121	0.0104	0.0088	0.0075	0.0065	0.0057	0.0051	0.0045	0.0041	0.0037	0.0033
0.4	0.0120	0.0103	0.0087	0.0075	0.0065	0.0057	0.0051	0.0045	0.0041	0.0037	0.0033
1	0.0119	0.0102	0.0086	0.0074	0.0065	0.0057	0.0050	0.0045	0.0040	0.0037	0.0033
2	0.0117	0.0100	0.0085	0.0073	0.0063	0.0056	0.0050	0.0044	0.0040	0.0036	0.0033
5	0.0112	0.0096	0.0082	0.0070	0.0061	0.0054	0.0048	0.0043	0.0039	0.0035	0.0032
10	0.0105	0.0091	0.0078	0.0067	0.0059	0.0052	0.0046	0.0042	0.0038	0.0034	0.0031
20	0.0098	0.0085	0.0073	0.0063	0.0056	0.0049	0.0044	0.0040	0.0036	0.0033	0.0030
40	0.0095	0.0083	0.0072	0.0063	0.0055	0.0049	0.0044	0.0040	0.0036	0.0033	0.0031

Table 12
REID (upper 95% confidence interval) accumulation rates, in %/day, for female astronauts exposed at an age of 50 years as a function of Al shielding thickness and solar modulation potential.

Al	Solar Modulation Potential, MV										
g/cm^2	420	500	600	700	800	900	1000	1100	1200	1300	1400
0.1	0.0180	0.0155	0.0130	0.0112	0.0097	0.0085	0.0075	0.0067	0.0060	0.0054	0.0049
0.4	0.0179	0.0154	0.0130	0.0111	0.0096	0.0084	0.0075	0.0067	0.0060	0.0054	0.0049
1	0.0177	0.0152	0.0128	0.0110	0.0095	0.0084	0.0074	0.0066	0.0059	0.0053	0.0049
2	0.0173	0.0149	0.0126	0.0108	0.0094	0.0083	0.0073	0.0065	0.0059	0.0053	0.0048
5	0.0164	0.0142	0.0120	0.0103	0.0090	0.0079	0.0070	0.0063	0.0057	0.0051	0.0047
10	0.0151	0.0131	0.0112	0.0097	0.0085	0.0075	0.0067	0.0060	0.0054	0.0049	0.0045
20	0.0138	0.0120	0.0103	0.0090	0.0079	0.0070	0.0063	0.0057	0.0051	0.0047	0.0043
40	0.0131	0.0115	0.0100	0.0087	0.0077	0.0069	0.0062	0.0056	0.0051	0.0047	0.0043

function of shielding thickness, and solar modulation potential. More plainly stated, these values represent the cumulative NASA effective dose an astronaut would incur upon reaching the 3% REID (at the upper 95% confidence interval) exposure limit if the entire exposure occurred under fixed conditions (i.e. no change in age, shielding thickness, or solar modulation potential). This representation removes the effects of the varying dose rates related to solar modulation potential, and instead highlights the influence of GCR spectral quality (as a function of sex, age, and shielding) on the relationship between NASA effective dose and probabilistic REID at the upper 95% confidence interval. According to Fig. 5, it is clear that the relationship between NASA effective dose and REID is not only complex, but unique for every permutation of sex, age, shielding thickness, and solar modulation potential.

6. Permissible mission duration (PMD)

NASA's PEL mandates a cumulative career maximum of 3% REID at the upper 95% confidence interval for any individual astronaut [NASA Human Integration Design Handbook, 2014]. In practice, a particular astronaut's accumulated career REID distribution over all prior missions must be included when determining the expected PMD for a mission-in-planning. However, since each astronaut's history is unique, and for the purpose of comparing relative risks, the maximum permissible mission duration is calculated in this work assuming the entire 3% limit is received in a single mission. Therefore, to calculate PMD, the limit of 3% REID is divided by the daily REID accumulation rate (at the upper 95% confidence interval) for a given solar modulation potential. The PMD values reported in this study correspond to free space environment scenarios such as interplanetary transit missions. Scenarios including proximal orbits of and/or surface intervals on celestial bodies would require further consideration of bulk shielding geometry and albedo radiation in the risk model calculations.

Figs. 6 and 7 illustrate permissible mission duration as a function of time and astronaut age for males and females, respectively. The shielding thickness used, 20 g/cm^2 Al, is representative of a free-space transit vessel (Crusan, 2015). The solid lines indicate PMD values calculated using the solar modulation potential timeseries observed by the CRaTER instrument. The dotted lines indicate times predating the LRO mission and are calculated using the Badhwar–O'Neill 2014 solar modulation potential timeseries.

Tables 13 and 14 specify the maximum and minimum free space PMD values for solar cycle 24, using the dose rates observed by the

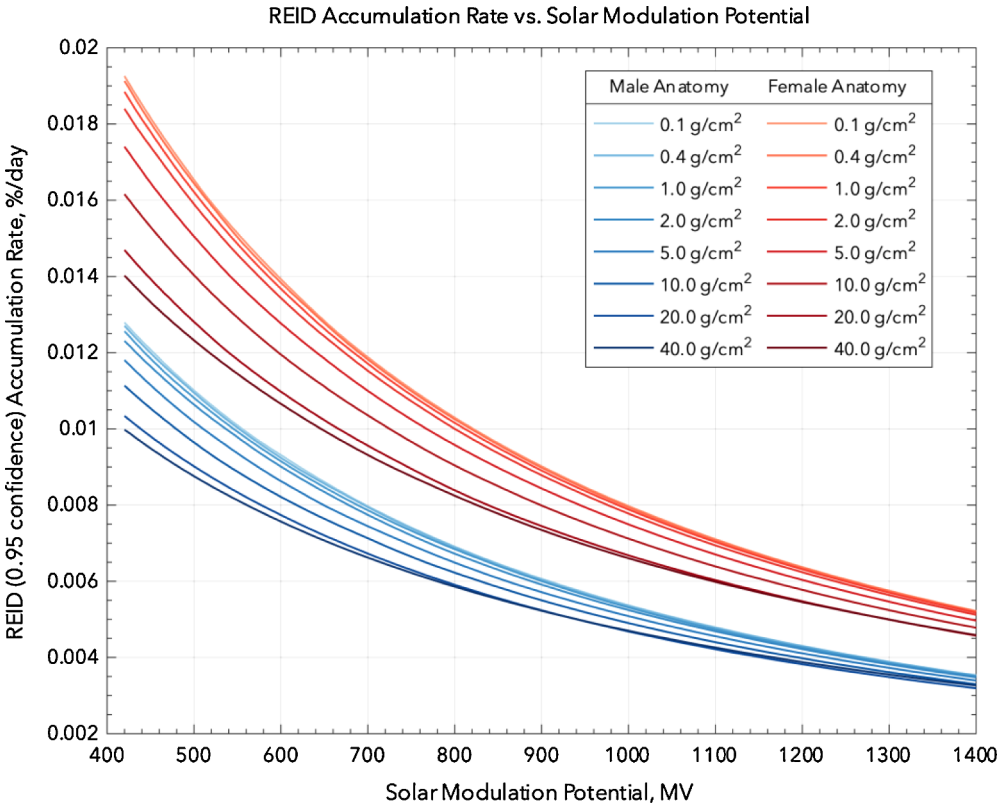

Fig. 4. REID Accumulation Rate vs. Solar Modulation Potential. The values are presented as a function of Al shield thickness and solar modulation potential. These results are valid for astronauts exposed at 45 years of age. Male and female astronauts are represented by the blue and red shades, respectively.

CRaTER instrument, as a function of astronaut age and shielding configuration for males and females, respectively. Note that within the context of this manuscript, the designation of minimum and maximum PMD refer to the minimum and maximum time intervals required to reach the allotted 3% REID at the upper 95% confidence interval limit. For 45-year-old male astronauts in a free-space transit spacecraft shielding configuration, the minimum and maximum PMD values during cycle 24 derived from observations made by the CRaTER instrument are 294 days and 466 days. For female astronauts in the same scenario, the minimum and maximum PMD values during cycle 24 derived from observations made by the CRaTER instrument are 207 days and 328 days.

The minimum PMD values derived from observations made by the CRaTER instrument during solar cycle 24 are, on average, within 3.5 days of the values reported by (Cucinotta et al., 2013). Fig. 8 provides historical context of how the conditions observed during solar cycle 24 compare with other cycles in recent history for 45-year-old male and female astronauts in a transit spacecraft shielding configuration. Furthermore, the historical minimum and maximum PMD values calculated using the Badhwar–O'Neill 2014 solar modulation potential timeseries are given in Tables 15 and 16. For 45-year-old male astronauts in a free-space transit spacecraft shielding configuration, the historical (>1750 CE) minimum and maximum PMD values are 290 days and 943 days. For female astronauts in the same scenario, the historical (>1750 CE) minimum and maximum PMD values are 204 days and 658 days.

Conclusions

The methodology shown here provides a means to verify and/or correct for solar activity effects in the current models used to project astronaut cancer risk using in-situ dose rates observed by the CRaTER instrument. A response function that links the known possible range of free space GCR conditions to onboard triple-coincident dose rate observations was derived using a series of Monte Carlo radiation transport calculations. This response function was used to obtain solar modulation potential timeseries from observed dose rates. The solar modulation potential timeseries obtained from CRaTER observations were compared with the expected values from the Badhwar–O'Neill 2014 model, which are derived from sunspot number observations.

Strong systematic agreement was observed between the GCR condition observed by CRaTER and the expected solar modulation potential timeseries given by the Badhwar–O'Neill 2014 model. However, the short-term effects of solar-born heliospheric transients on the GCR condition are captured by the CRaTER observations but are largely missing from model timeseries derived from sunspot number observations. One example of such an effect is the local minimum in observed dose rate associated with the increase in GCR modulation from the September 2017 series of events. The Badhwar–O'Neill 2014 solar modulation timeseries also consistently overestimates the observed dose rate during the period of transition from solar maximum to solar minimum (roughly 2015 through 2018). Since CRaTER measures changes in the near-Earth deep space GCR condition directly, it is uniquely well suited to provide a reference observation for cancer risk model projections.

The CRaTER instrument possesses two unique advantages that make it an ideal reference observer of the local GCR condition for biological risk evaluation. The first advantage is its ability to observe the GCR condition at Earth's position in the heliosphere in near real-time, while remaining largely beyond the influence of the Earth's magnetosphere. The second advantage, while not immediately evident, lies within CRaTER's TEP-inclusive design, which inherently measures the most biologically significant component of the GCR spectrum when the coincidence conditions used in this study are applied. It is important to note the distinction between the biologically relevant GCR flux (measured in triple coincidence dose rates) and the less energetic portion of

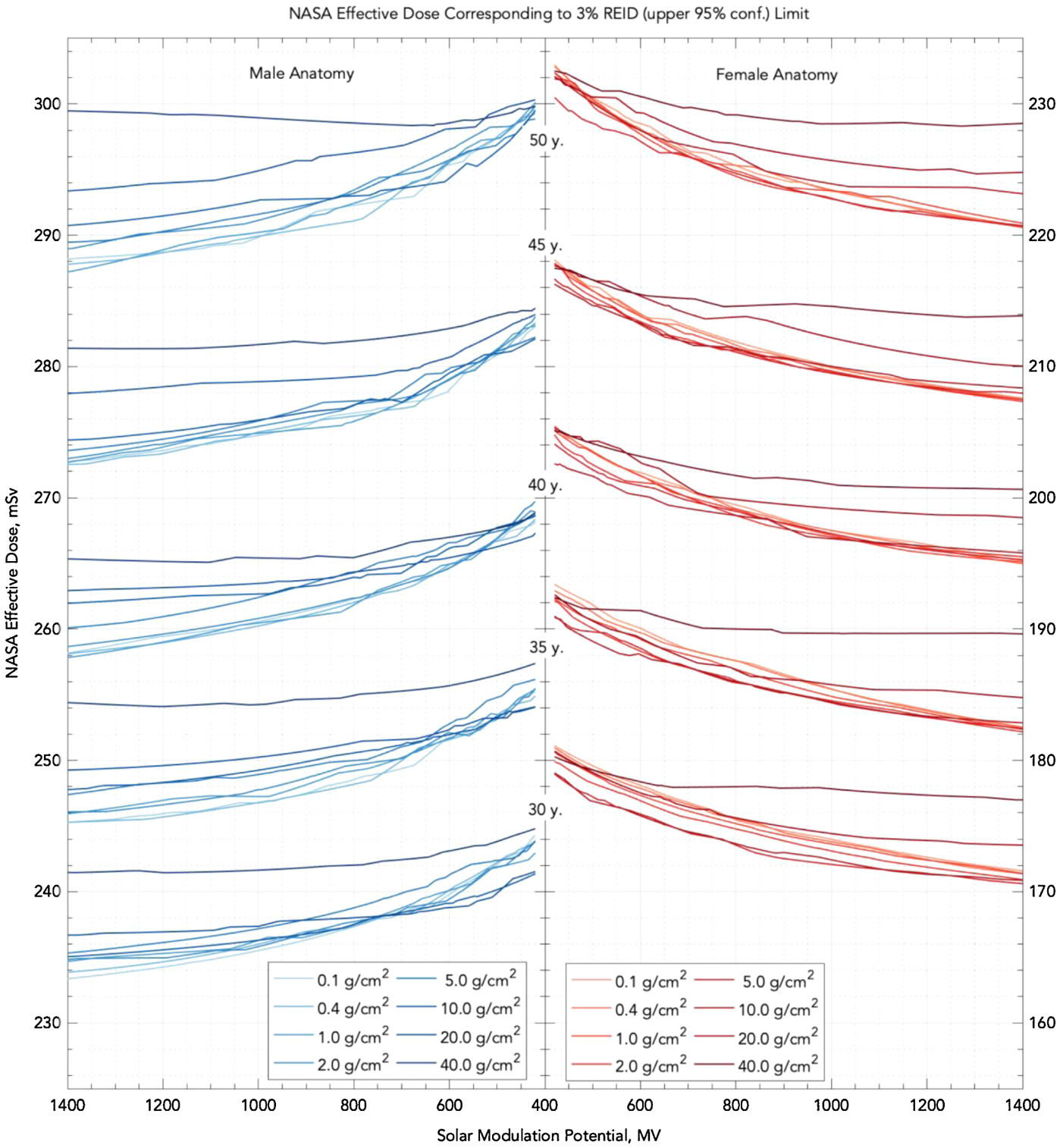

Fig. 5. NASA Effective Dose Corresponding to 3% REID (upper 95% conf.) Limit. The values are presented as a function of Al shield thickness, solar modulation potential, and astronaut age at exposure. Male (left) and female (right) astronauts are represented by the blue and red shades, respectively. Note that the ordinate range of the right (female) plot is different from the left plot (male).

the GCR spectrum (measured in double, or no, coincidence dose rates). A particle that passes through all three detector pairs, including both TEP volumes, must penetrate at least 8.44 g/cm^2 of material. However, a minimum of only 0.49 g/cm^2 must be penetrated to pass through the first detector pair (D1, D2).

Consequently, the dose rates observed in the third detector pair via triple coincidence are measurements of the biologically significant portion of the GCR spectrum (proton energies greater than 114.5 MeV). The dose rates observed via single events in the first detector pair include GCR protons with energies as low as 12.7 MeV. This includes the GCR energy regime that is not only most strongly influenced by small changes in solar activity and therefore the least predictable, but also the least significant in terms of human risk. According to Slaba and Blattnig (2014), the relative NASA effective dose contribution of GCR

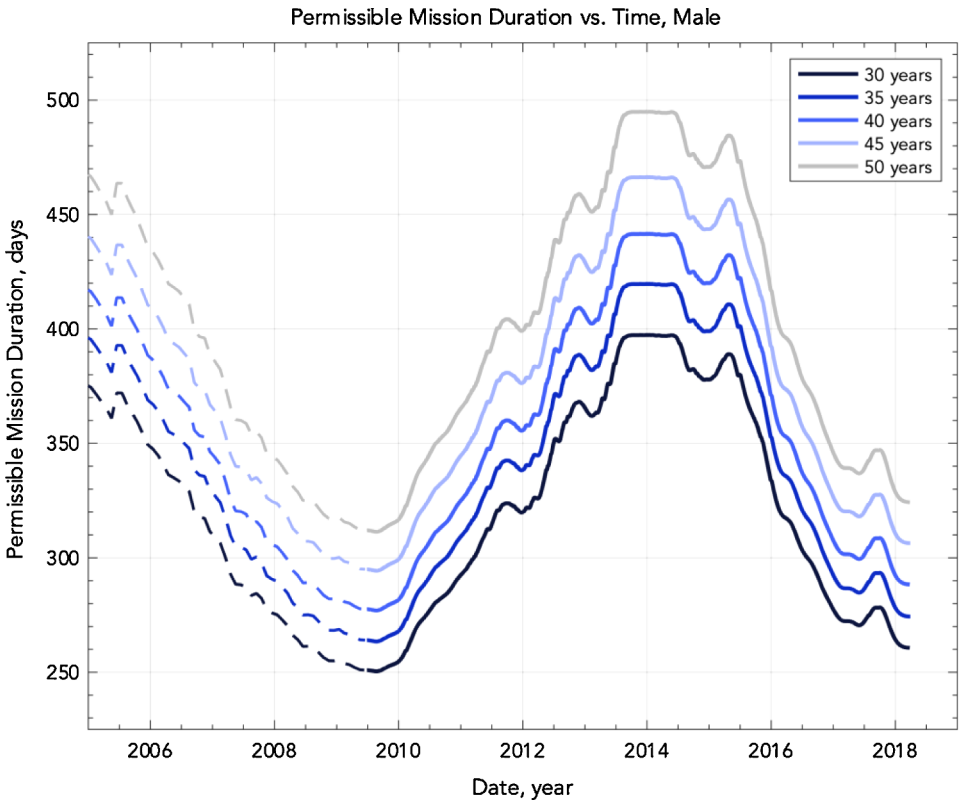

Fig. 6. Permissible Mission Duration (PMD) vs. Time, Male. PMD timeseries for male astronauts as a function of age at exposure according to the 3% REID limit at the upper 95% confidence level. These values apply to deep space conditions at 1 AU behind 20 g/cm^2 Al shielding. Values before June 2009 (dashed) are calculated from the Badhwar–O'Neill 2014 solar modulation potential timeseries. Values after June 2009 (solid) are calculated using the solar modulation potential observed by the CRaTER instrument.

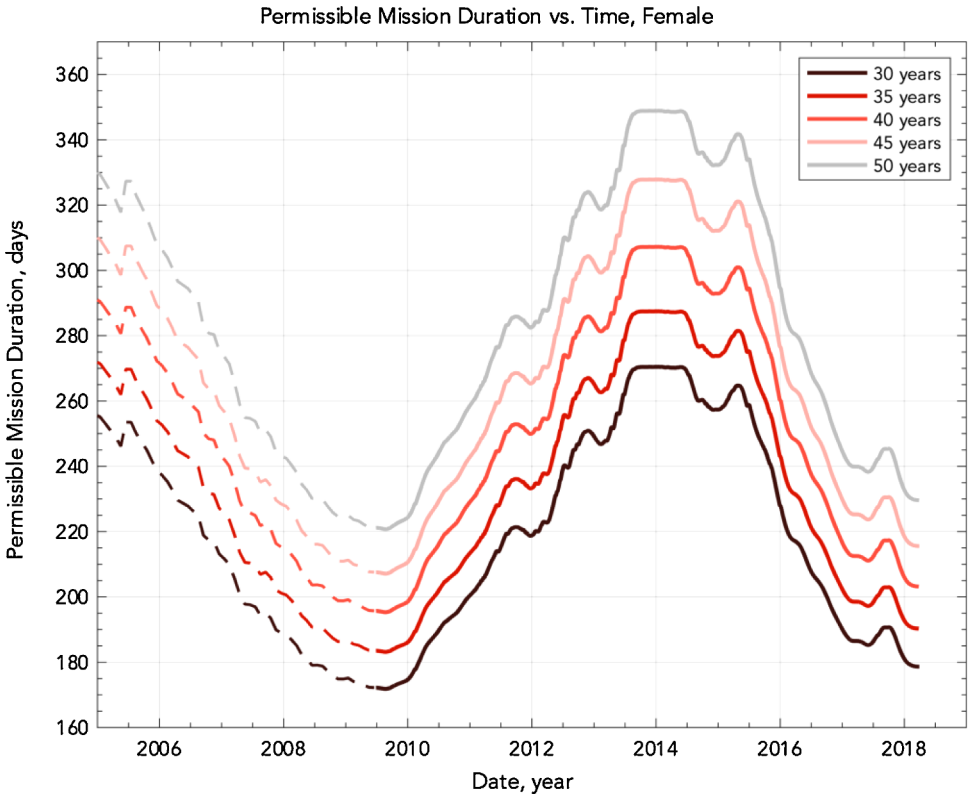

Fig. 7. Permissible Mission Duration (PMD) vs. Time, Female. PMD timeseries for female astronauts as a function of age at exposure according to the 3% REID limit at the upper 95% confidence level. These values apply to deep space conditions at 1 AU behind 20 g/cm^2 Al shielding. Values before June 2009 (dashed) are calculated from the Badhwar–O'Neill 2014 solar modulation potential timeseries. Values after June 2009 (solid) are calculated using the solar modulation potential observed by the CRaTER instrument.

particles with incident energies less than 250A MeV is 10% of the total for a completely unshielded astronaut and quickly drops to 2.5% and 0.3% of the total for shielded scenarios with 20 g/cm^2 Al and 40 g/cm^2 Al, respectively.

Furthermore, the fluxes predicted by the Badwhar-O'Neill 2014 GCR model are reported by O'Neill et al., 2015 to differ from observations by a 13% average absolute relative difference over all energies. However, it is important to note that the agreement between the modeled and measured GCR fluxes is weakest for energies less than 250A MeV and strongest for energies greater than 250A MeV. Previous investigations

Table 13
Minimum and maximum permissible mission duration values, in days, for male astronauts during solar cycle 24 derived from observations by the CRaTER instrument. These values apply to deep space conditions and are presented as a function of the astronaut's age at exposure as well as spacecraft shielding thickness.

Al	30 years		35 years		40 years		45 years		50 years	
g/cm^2	min.	max.	min.	max.	min.	max.	min.	max.	min.	max.
0.1	205	340	215	356	226	375	238	395	252	418
0.4	206	342	216	357	227	377	240	397	253	419
1	208	345	219	361	230	381	243	400	257	424
2	213	349	223	367	235	386	247	407	261	432
5	223	364	234	381	246	403	258	422	273	447
10	234	379	246	399	260	420	273	441	290	467
20	250	397	263	420	277	442	294	466	311	495
40	262	406	276	427	288	446	305	473	321	500

Table 14
Minimum and maximum permissible mission duration values, in days, for female astronauts during solar cycle 24 derived from observations by the CRaTER instrument. These values apply to deep space conditions and are presented as a function of the astronaut's age at exposure as well as spacecraft shielding thickness.

Al	30 years		35 years		40 years		45 years		50 years	
g/cm^2	min.	max.	min.	max.	min.	max.	min.	max.	min.	max.
0.1	131	220	140	235	149	250	158	265	169	282
0.4	132	221	141	236	150	251	159	267	170	283
1	134	223	143	238	152	253	162	269	173	286
2	137	226	146	241	155	258	166	273	177	291
5	144	236	154	252	165	270	175	286	186	305
10	156	250	166	268	177	286	188	304	202	325
20	172	270	183	287	195	307	207	328	221	349
40	180	278	192	297	204	316	217	336	232	359

Table 15
Minimum and maximum permissible mission duration values, in days, calculated from the Badhwar–O'Neill 2014 model from 1750 to 2018 CE for male astronauts. These values apply to deep space conditions and are presented as a function of the astronaut's age at exposure as well as spacecraft shielding thickness.

Al	30 years		35 years		40 years		45 years		50 years	
g/cm^2	min.	max.	min.	max.	min.	max.	min.	max.	min.	max.
0.1	202	729	211	766	222	807	234	852	248	901
0.4	203	733	212	768	224	809	236	854	249	902
1	205	739	215	774	227	812	239	859	253	904
2	209	745	219	781	231	821	244	867	258	917
5	220	763	231	802	243	843	254	887	269	939
10	230	782	243	824	257	871	269	913	286	967
20	247	803	260	846	273	892	290	943	307	996
40	259	791	272	834	284	869	301	922	317	981

Table 16
Minimum and maximum permissible mission duration values, in days, calculated from the Badhwar–O'Neill 2014 model from 1750 to 2018 CE for female astronauts. These values apply to deep space conditions and are presented as a function of the astronaut's age at exposure as well as spacecraft shielding thickness.

Al	30 years		35 years		40 years		45 years		50 years	
g/cm^2	min.	max.	min.	max.	min.	max.	min.	max.	min.	max.
0.1	129	477	138	507	147	543	156	577	166	613
0.4	130	478	139	509	148	544	157	579	168	615
1	132	481	141	512	150	548	159	582	170	620
2	135	485	144	516	153	554	163	588	174	626
5	142	497	152	532	162	569	172	606	183	644
10	154	517	164	553	174	592	186	630	199	675
20	169	544	181	579	193	622	204	658	218	705
40	177	543	189	582	202	616	214	656	229	701

indicating a 10% enhancement in the dose rates observed by the CRaTER instrument above expected values during the transitionary period from solar maximum to solar minimum in cycle 24 utilize the first detector pair (D1, D2) (Schwadron et al., 2014, 2018). While the disparity between the thinly shielded observed dose rates and expected values is not unreasonable considering the known uncertainties within the Badhwar–O'Neill 2014 model, observations of triple-coincident dose rates provide a more accurate evaluation of the GCR condition for the purposes of quantifying radiobiological risk.

The PMD of deep space human operations associated with the GCR environment were calculated using NASA's probabilistic risk model. The PMD values are based on the NASA radiobiological career risk limit of 3% REID at the upper 95% confidence interval. The HZETRN code was used to calculate NASA effective doses and REID for the MAX and FAX human phantoms exposed to various GCR boundary conditions. Tables are provided for both NASA effective dose and REID accumulation rates as a function of Badhwar–O'Neill 2014 solar modulation potential. PMD as a function of time was obtained by applying the

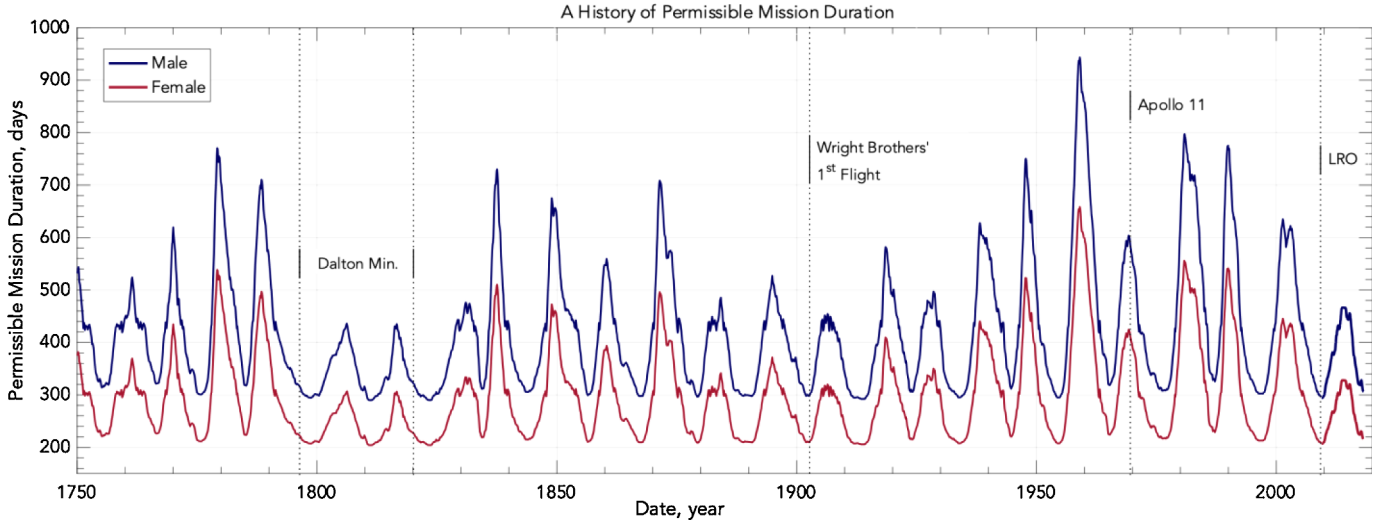

Fig. 8. A History of Permissible Mission Duration (PMD). These timeseries represent permissible mission duration in deep space conditions from 1750 CE to 2018 CE for 45-year-old male (blue) and female (red) astronauts behind 20 g/cm^2 Al shielding. Values before June 2009 are calculated from the Badhwar–O'Neill 2014 solar modulation potential timeseries. Values after June 2009 are calculated using the solar modulation potential observed by the CRaTER instrument.

output of the risk model to the solar modulation potential timeseries observed by the CRaTER instrument for solar cycle 24. A historical account of PMD was calculated based upon the sunspot number derived Badhwar–O'Neill 2014 solar modulation potential timeseries. Tables are provided containing minimum and maximum PMD for both the directly observed solar cycle 24 and the historical reconstruction.

As expected, PMD increases with both shielding thickness and age at exposure. At large shielding thickness, the radiation field is increasingly dominated by neutrons and light ions. The nuclear production cross sections for these particles remains highly uncertain due to lack of experimental data, and transport approximation error may also be significant for these particles beyond ~30 g/cm^2 of shielding. More detailed discussion of these issues is provided by Slaba et al. (2017). Minimum PMD values for 30-year-old astronauts were observed to be roughly between 75–80% of the PMD for 50-year-old astronauts in the same setting. During solar cycle 24, the minimum PMD for astronauts behind 20 g/cm^2 Al was observed to range from 250 days to 311 days for males and 172 days to 221 days for females. The maximum PMD during solar cycle 24 for astronauts behind 20 g/cm^2 Al was observed to range from 397 days to 495 days for males and 270 days to 349 days for females. The historical minimum PMD for astronauts behind 20 g/cm^2 Al for males was observed to range from 247 days to 307 days for males and 169 days to 218 days for females. The historical maximum PMD for astronauts behind 20 g/cm^2 Al for males was observed to range from 803 days to 996 days for males and 544 days to 705 days for females.

To put these PMD values into perspective it is worth comparing these durations with various other relevant human exploration timescales. For lunar exploration, mission durations are planned to be far shorter than the minimum PMDs found above. Mars missions are potentially a different story. The lowest energy orbit from Earth to rendezvous with Mars is a Hohmann transfer orbit. That orbit takes approximately nine months from Earth to Mars. Once at Mars, one would have to wait another approximately 16 months for favorable transfer geometry on another Hohmann orbit back to Earth. The return trip would also take nine months. Clearly a full mission scenario of deep space travel of 18 months (let alone 16 additional months on the similarly shielded Martian surface) poses a challenge, given that mission duration exceeds all predicted PMDs. This argues for higher-energy orbits, calling for missions that involve on-orbit staging. Such missions have been proposed with roundtrip durations as short as 245 days (Folta et al., 2012); such mission durations are marginally compatible with the shortest PMDs expected during historic intense solar maxima for male astronauts, but not necessarily for female astronauts.

The minimum PMD for any given configuration of sex, shielding, and age is fairly consistent across all solar cycles, while the maximum PMD may vary drastically between any two cycles. It should be noted that the PMD calculations reported in this work do not include the additional risk presented by doses imparted by potential SEP events. It is worth remembering that when the risks from ionizing radiation owing to GCR are at their lowest (solar maximum), the risks from SEPs are at their highest; although current shield design and optimization strategies are capable of mitigating most of the SEP exposure and risk. The authors intend to continue this work by extending this analysis to include the lunar orbit environment, as would be appropriate for a deep space gateway.

Declaration of Competing Interest

None.

Acknowledgments

This work was performed under the auspices of NASA grant number NNG11PA03C. CRaTER data are available at http://crater-web.sr.unh.edu.

References

Ackermann, M., Ajello, M., Allafort, A., Baldini, L., Ballet, J., Barbiellini, G., …, Zimmer, S., 2013. Detection of the characteristic pion-decay signature in supernova remnants. Science 339 (6121), 807–811. https://doi.org/10.1126/science.1231160.

Boice Jr., J.D., Ellis, E.D., Golden, A.P., Zablotska, L.B., Mumma, M.T., Cohen, S.S., 2019. Sex-specific lung cancer risk among radiation workers in the million-person study and patients TB-fluoroscopy. Int. J. Radiat. Biol. 1–12. https://doi.org/10.1080/09553002.2018.1547441.

Goorley, T., James, M., Booth, T., Brown, F., Bull, J., Cox, L.J., …, Zukaitis, T., 2012. Initial MCNP6 release overview. Nucl. Technol. 180 (3), 298–315. https://doi.org/10.13182/nt11-135.

Iskra, K., Siluszyk, M., Alania, M., Wozniak, W., 2019. Experimental investigation of the delay time in galactic cosmic ray flux in different epochs of solar magnetic cycles: 1959 – 2014. Sol. Phys. 294 (9). https://doi.org/10.1007/s11207-019-1509-4.

Kim, M.-H.Y., Hayat, M.J., Feiveson, A.H., Cucinotta, F.A., 2009. Prediction of frequency and exposure level of solar particle events. Health Phys. 97 (1), 68–81. https://doi.org/10.1097/01.hp.0000346799.65001.9c.

Kramer, R., Khoury, H.J., Vieira, J.W., Loureiro, E.C.M., Lima, V.J.M., Lima, F.R.A., Hoff, G., 2004. All about FAX: a female adult voXel phantom for Monte Carlo calculation in radiation protection dosimetry. Phys. Med. Biol. 49 (23), 5203–5216. https://doi.org/10.1088/0031-9155/49/23/001.

Kramer, R., Vieira, J.W., Khoury, H.J., Lima, F.R.A., Fuelle, D., 2003. All about MAX: a male adult voxel phantom for Monte Carlo calculations in radiation protection dosimetry. Phys. Med. Biol. 48 (10), 1239–1262. https://doi.org/10.1088/0031-9155/48/10/301.

Looper, M.D., Mazur, J.E., Blake, J.B., Spence, H.E., Schwadron, N.A., Golightly, M.J., …, Townsend, L.W., 2013. The radiation environment near the lunar surface: CRaTER observations and GEANT4 simulations. Space Weather 11 (4), 142–152. https://doi.org/10.1002/swe.20034.

Luhmann, J.G., Mays, M.L., Li, Y., Lee, C.O., Bain, H., Odstrcil, D., …, Petrie, G., 2018. Shock connectivity and the late cycle 24 solar energetic particle events in July and September 2017. Space Weather 16 (5), 557–568. https://doi.org/10.1029/2018sw001860.

Cucinotta, F.A., Y. Kim, M.-H., & Chappell, L.J., 2013. Space radiation cancer risk projections and uncertainties – 2012. NASA/TP 2013-217375. https://doi.org/10.13140/rg.2.1.1413.3528.

Folta, D.C., Vaughn, F.J., Rawitscher, G.S., Westmeyer, P.A., 2012. Fast Mars transfers through on-orbit staging, concepts and approaches for Mars exploration, held June 12-14, 2012 in Houston, Texas. LPI Contribution No. 1679, id.4181. https://www.lpi.usra.edu/meetings/marsconcepts2012/pdf/4181.pdf.

NASA human integration design handbook, 2014. NASA/SP-2010-3407/REV1, https://www.nasa.gov/sites/default/files/atoms/files/human_integration_design_handbook_revision_1.pdf.

Matthiä, D., Hassler, D.M., de Wet, W., Ehresmann, B., Firan, A., Flores-McLaughlin, J., …, Zeitlin, C., 2017. The radiation environment on the surface of Mars - summary of model calculations and comparison to RAD data. Life Sci. Space Res. (Amst) 14, 18–28. https://doi.org/10.1016/j.lssr.2017.06.003.

Matthiä, D., Meier, M.M., Berger, T., 2018. The solar particle event on 10-13 september 2017: spectral reconstruction and calculation of the radiation exposure in aviation and space. Space Weather 16 (8), 977–986. https://doi.org/10.1029/2018sw001921.

Mossman, K.L., 2012. NCRP report 167: potential impact of individual genetic susceptibility and previous radiation exposure on radiation risk for astronauts. Health Phys. 102 (1), 101–102. https://doi.org/10.1097/hp.0b013e3182295960.

Norbury, J.W., Slaba, T.C., Sobolevsky, N., Reddell, B., 2017. Comparing HZETRN, SHIELD, FLUKA and GEANT transport codes. Life Sci. Space Res. (Amst) 14, 64–73. https://doi.org/10.1016/j.lssr.2017.04.001.

Nymmik, R.A., Suslov, A.A., 1995. Characteristics of galactic cosmic ray flux lag times in the course of solar modulation. Advances in Space Research 16 (9), 217–220. https://doi.org/10.1016/0273-1177(95)00338-f.

O'Neill, P.M., Golge, S., Slaba, T.C., 2015. Badhwar–O'Neill 2014 galactic cosmic ray flux model description. Tech. Rep. NASA/TP-2015-218569.. https://ntrs.nasa.gov/archive/nasa/casi.ntrs.nasa.gov/20150003026.pdf.

Schwadron, N.A., Blake, J.B., Case, A.W., Joyce, C.J., Kasper, J., Mazur, J., …, Zeitlin, C., 2014. Does the worsening galactic cosmic radiation environment observed by CRaTER preclude future manned deep space exploration? Space Weather 12 (11), 622–632. https://doi.org/10.1002/2014sw001084.

Schwadron, N.A., Rahmanifard, F., Wilson, J., Jordan, A.P., Spence, H.E., Joyce, C.J., …, Zeitlin, C., 2018. Update on the worsening particle radiation environment observed by CRaTER and implications for future human deep-space exploration. Space Weather 16 (3), 289–303. https://doi.org/10.1002/2017sw001803.

Slaba, T.C., Qualls, G.D., Clowdsley, M.S., Blattnig, S.R., Walker, S.A., Simonsen, L.C., 2010a. Utilization of CAM, CAF, MAX, and FAX for space radiation analyses using HZETRN. Adv. Space Res. 45 (7), 866–883. https://doi.org/10.1016/j.asr.2009.08.017.

Slaba, T.C., Blattnig, S.R., Badavi, F.F., 2010b. Faster and more accurate transport procedures for HZETRN. J. Comput. Phys. 229 (24), 9397–9417. https://doi.org/10.1016/j.jcp.2010.09.010.

Slaba, T.C., Blattnig, S.R., Aghara, S.K., Townsend, L.W., Handler, T., Gabriel, T.A., …, Reddell, B., 2010c. Coupled neutron transport for HZETRN. Radiat. Meas. 45 (2), 173–182. https://doi.org/10.1016/j.radmeas.2010.01.005.

Slaba, T.C., Blattnig, S.R., 2014. GCR environmental models I: sensitivity analysis for GCR environments. Space Weather 12 (4), 217–224. https://doi.org/10.1002/2013sw001025.

Slaba, T.C., Bahadori, A.A., Reddell, B.D., Singleterry, R.C., Clowdsley, M.S., Blattnig,

S.R., 2017. Optimal shielding thickness for galactic cosmic ray environments. Life Sci. Space Res. 12, 1–15. https://doi.org/10.1016/j.lssr.2016.12.003.

Spence, H.E., Case, A.W., Golightly, M.J., Heine, T., Larsen, B.A., Blake, J.B., …, Charara, Y., 2010. CRaTER: the cosmic ray telescope for the effects of radiation experiment on the lunar reconnaissance orbiter mission. Space Sci. Rev. 150 (1–4), 243–284. https://doi.org/10.1007/s11214-009-9584-8.

Spence, H.E., Golightly, M.J., Joyce, C.J., Looper, M.D., Schwadron, N.A., Smith, S.S., …, Zeitlin, C., 2013. Relative contributions of galactic cosmic rays and lunar proton "albedo" to dose and dose rates near the moon. Space Weather 11 (11), 643–650. https://doi.org/10.1002/2013sw000995.

Townsend, L.W., Charara, Y.M., Delauder, N., PourArsalan, M., Anderson, J.A., Fisher, C.M., …, Cucinotta, F.A., 2010. Parameterizations of the linear energy transfer spectrum for the CRaTER instrument during the LRO mission. Space Weather 8 (3). https://doi.org/10.1029/2009sw000526.

Trump, D.J., 2017. Presidential memorandum on reinvigorating America's human space exploration program [Memorandum]. Office of the Federal Register, National Archives and Records Administration, Washington, DC. https://www.whitehouse.gov/presidential-actions/presidential-memorandum-reinvigorating-americas-human-space-exploration-program/.

Crusan, J., 2015. Evolvable Mars campaign and technology development. https://www.nasa.gov/sites/default/files/files/4-Status_of_EMC(1).pdf.

NASA strategic plan 2018, 2018. https://www.nasa.gov/sites/default/files/atoms/files/nasa_2018_strategic_plan.pdf.

Usoskin, I.G., Kananen, H., Mursula, K., Tanskanen, P., Kovaltsov, G.A., 1998. Correlative study of solar activity and cosmic ray intensity. J. Geophys. Res. 103 (A5), 9567–9574. https://doi.org/10.1029/97ja03782.

Warner, J.E., Norman, R.B., Blattnig, S.R., 2018. HZETRN radiation transport validation using balloon-based experimental data. Life Sci. Space Res. 17, 23–31. https://doi.org/10.1016/j.lssr.2018.02.003.

NASA standard 3001, volume 2, 2015. NASA/STD-3001/REVA, https://www.nasa.gov/sites/default/files/atoms/files/nasa-std-3001-vol-2a.pdf.

Wilson, J.W., Townsend, L.W., Schimmerling, W., Khandelwal, G.S., Khan, F., Nealy, J.E., Cucinotta, F.A., Simonsen, L.C., Shinn, J.L., & Norbury, J.W., 1991. Transport methods and interactions for space radiations. NASA/RP-1257. https://ntrs.nasa.gov/archive/nasa/casi.ntrs.nasa.gov/19920006738.pdf.